Mineralogical Magazine, October 2017, Vol. 81(5), pp. 1087–1104

Complex exsolution microstructures in ilmenite–pyrophanite from the Garnet Codera dyke pegmatite (Central Italian Alps): an electron microscopy investigation

Gian Carlo Capitani

Department of Earth and Environmental Sciences, University of Milano-Bicocca, P.za della Scienza, 4, 20126 Italy

[*Received 13 June 2016; Accepted 28 September 2016; Associate Editor: Andrew Christy*]

ABSTRACT

Ilmenite–pyrophanite crystals from a garnet pegmatite dyke from the Upper Codera Valley (Sondrio, Italian Alps) showing exsolutions of titanohematite and columbite–tantalite were investigated by scanning and transmission electron microscopy. The titanohematite precipitates share the same crystallographic orientation of the ilmenite–pyrophanite host, are bean-shaped when observed on sections inclined to the pinacoidal section, and are elongated when observed on sections closer to the prism section, possibly because of their discoidal shape parallel to (001). The columbite–tantalite precipitates form a hexagonal network of needles elongated along ⟨110⟩ of the ilmenite–pyrophanite and titanohematite host. The following crystallographic relationship was established: $[100]_{Col}//[001]_{Ilm}$; $[001]_{Col}//\langle 110\rangle_{Ilm}$; $[010]_{Col}//\langle \bar{1}10\rangle_{Ilm}$, which can be explained in terms of preservation of the oxygen close packing between the ilmenite and columbite structures. The interfaces between any two of the three different phases are coherent but show lattice strain contrast and sometimes dislocations because of their different unit-cell dimensions. On the basis of textural observations, titanohematite is supposed to exsolve first, followed by columbite–tantalite at temperatures below 500°C. The addition of MnO to the Fe_2O_3–$FeTiO_3$ system is supposed to considerably influence the topology of the related *T*–*X* phase diagram and the solubility of Nb_2O_5 and Ta_2O_5 in this system.

Keywords: ilmenite, pyrophanite, titanohematite, columbite, tantalite, exsolution, transmission electron microscopy.

Introduction

Ilmenite ($FeTiO_3$) forms complete solid solutions at high temperature with pyrophanite ($MnTiO_3$), geikielite ($MgTiO_3$) and hematite (Fe_2O_3) (Gaspar and Wyllie, 1983; Zaccarini *et al.*, 2004). Minerals of the ilmenite–hematite solid solution series are common accessory minerals in a variety of igneous, metamorphic and sedimentary rocks and have widespread importance in petrology, as they can provide, in conjunction with other coexisting Fe-bearing phases, information on oxygen fugacity, crystallization temperatures and cooling rates (Evans *et al.*, 2006). The pyrophanite-dominant phase is relatively less abundant in Nature. It is typical of sedimentary and metamorphosed Mn deposits, evolved siliceous and peralkaline silica-undersaturated rocks, and carbonatites (Gaspar and Wyllie, 1983; Mitchell and Liferovich, 2004; Zaccarini *et al.*, 2004).

Ilmenite and hematite can play an important role in the acquisition of rock magnetization. Magnetic minerals are of significant interest in many different fields of geological science because of their capacity to retain memory of the geomagnetic field that was present during the formation of the rock. The most extraordinary application of the paleomagnetic information contained in magnetic minerals is the mapping of the movement of

E-mail: giancarlo.capitani@unimib.it
https://doi.org/10.1180/minmag.2016.080.154

continental and oceanic plates, one of the most convincing proofs of the Plate-tectonic theory.

Recently, it has been discovered in several localities that rocks containing finely exsolved hematite–ilmenite microstructures create large remanence-dominated magnetic anomalies (McEnroe *et al.*, 2001, 2002), and on the basis of these observations the theory of 'lamellar-magnetism' has been developed (Robinson *et al.*, 2002, 2004). According to this theory, mixed-valence contact layers form at the hematite–ilmenite interface to reduce local charge imbalance, and these layers convey a net $\approx 4\ \mu_B$ per lamella ($1\ \mu_B$ = one Bohr magneton = 9.274×10^{-24} Am^2), such that the total intensity of lamellar magnetism, when the moments of individual lamellae are magnetically aligned, is proportional to the density and surface area of lamellae. The lamellar magnetism is very stable and resistant to demagnetization in alternating fields normally 1000 times more intense than that of the Earth, making it an ideal candidate for the generation of ancient crust magnetic anomalies. Moreover, experimental studies at 10 kbar and 580°C demonstrate that lamellar magnetism is not demagnetized, as is the case for magnetite, the other major source of remanent anomalies (McEnroe *et al.*, 2004), suggesting that it could be the source of deep crustal magnetic anomalies.

From a structural point of view, ilmenite, pyrophanite and hematite share the same rhombohedral structure based on the corundum HCP oxygen packing scheme. It can be described in terms of octahedral sites laying parallel to (001), hosting Fe^{3+} in hematite, and Fe^{2+} (or Mn^{2+}) and Ti^{4+} in alternate layers in ilmenite (pyrophanite). The doubling of crystallographically non-equivalent cations reduces the symmetry from $R\bar{3}c$ in hematite to $R\bar{3}$ in ilmenite. Only two-thirds of the sites are occupied, leading to an A_2O_3 stoichiometry. Within a layer, each occupied octahedron shares two oxygens (an edge) with the neighbours forming connected six-fold rings. Successive octahedral layers share a common oxygen layer and are arranged so that each occupied octahedron in adjacent layers shares three oxygen anions (a face) and are shifted in adjacent upper and lower neighbouring layers (Fig. 1*a* and *c*). The repeat distance along **c** comprises six layers. Columbite-group oxides have basic stoichiometry AB_2O_6, where A is usually Fe^{2+} and B = Nb^{5+} in columbite, and A = Mn^{2+} and B = Ta^{5+} in tantalite, but many other substitutions are possible, especially with tetravalent cations such as Ti^{4+} and Sn^{4+}. The columbite structure (*Pbcn*) is a derivative of the α-PbO_2 structure based on a HCP oxygen arrangement. It can be described in terms of octahedral layers, in this case made of zig-zag chains of edge-sharing octahedra running along [001] and parallel to (100). Two different chains correspond to the A and B sites, each constituting a different layer (Fig. 1*b* and *d*). Iron, Mn, Nb and Ta are usually disordered over the A and B sites, but may undergo ordering, for instance upon heating, with bivalent cations preferring the A site and pentavalent cations the B sites. The resulting ABBABB ordering sequence entails a tripling of the *a* cell parameter, leading to a tri-α-PbO_2-type structure in which *Pbcn* symmetry is maintained (Tarantino *et al.*, 2011).

In this paper, we describe microscopic titanohematite precipitates in ilmenite–pyrophanite crystals from the Garnet Codera pegmatites (Italian Alps). In addition to exsolved Ti-rich hematite in perfect crystallographic orientation with the host, we found exsolved columbite–tantalite needles with elongation direction parallel to the three ⟨110⟩ axes of the rhombohedral phases. The contacts of any two of these three phases were studied by high-resolution transmission electron microscopy (HRTEM) along different observation directions and their reciprocal crystallographic orientation rationalized on the basis of their crystal structure. Possible effects of manganese addition to the Fe_2O_3–$FeTiO_3$ system are discussed.

Geological outline, samples and methods

The pegmatite dyke studied belongs to a swarm of pegmatite dykes cropping out along the ancient glacial circle located in the upper Codera Valley, Sondrio (Central-Western Italian Alps) that intrude the main granodiorite body ('Ghiandone') of the Masino-Bregaglia pluton, the transition zone towards the outer tonalite rim ('Serizzo'), and the surrounding metamorfites (Fig. 2; De Michele and Zezza, 1979, Bedogné *et al.*, 1995, Guastoni *et al.*, 2014). Dykes were emplaced during the syn-magmatic stage above 500°C, which was characterized by a pervasive solid-state foliation and circulation of late-stage hydrothermal fluids. Crosscutting relationships indicate the presence of more than a single generation of pegmatite dykes. Age determination using U-Th-Pb on monazite and xenotime indicate an average emplacement age of 25–26 Ma (Guastoni, unpublished data). The dyke studied outcrops for 30 m, reaches up to 3 m wide, and shows boudins and lobate structures along

https://doi.org/10.1180/minmag.2016.080.154 Published online by Cambridge University Press

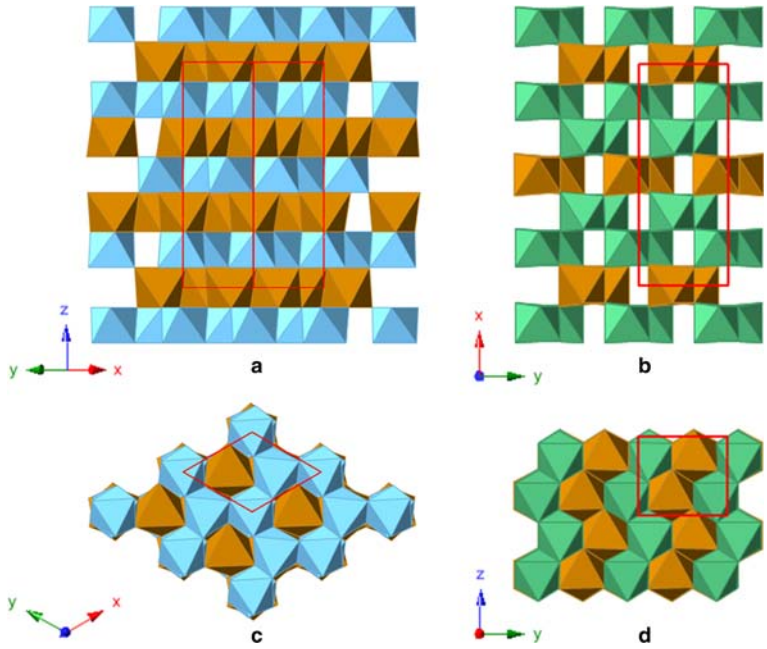

FIG. 1. The ilmenite structure as seen down [110] (*a*) and [001] (*c*) and the columbite structure as seen down [001] (*b*) and [100] (*d*). The projections have been drawn according to their crystallographic relationship. Note the parallelism between the octahedral layers (*a vs. b*) and between the octahedral chains (*c vs. d*). Blue = Ti sites; brown = Fe sites (ilmenite) or A sites (columbite); green = B sites.

contacts with enclosing rocks. It shows symmetric core-border zoning in the mineral assemblage, which is constituted mainly by perthitic K-feldspar and quartz, both in crystals elongated along the strike of the dyke because of the occurrence of intense ductile deformation during emplacement. Red garnet and beryl (aquamarine) are present in the core zone; quartz + K-feldspar graphic textures may be dominant in the wall-intermediate zone; magnetite and spessartine also occur in this zone; biotite flakes forming comb textures are present in the border-wall zone, along with rare-earth element (*REE*)-U bearing minerals such as (Y-*REE*-U-Th)-(Nb-Ta-Ti) oxides, uraninite, monazite-(Ce) and zircon (Guastoni *et al.*, 2014; Capitani *et al.*, 2016).

Several millimetre sized, oxide-bearing rock fragments from the border-wall zone hand specimens were attached to an aluminium stub, carbon coated, and first studied with a scanning electron microscope (SEM). On the basis of qualitative compositional spectra and back-scattered electron (BSE) images, two crystal aggregates containing ilmenite–pyrophanite were selected, embedded in epoxy, polished on the one side, carbon coated and further studied by SEM for semi-quantitative energy dispersive (EDS) chemical analyses. After this step, the samples were sectioned with a diamond wheel, mechanically milled down to 30 μm, polished on the other side, then ion milled down to electron transparency.

The SEM-EDS investigations were performed at the Earth and Environmental Sciences Department of the University of Milano-Bicocca with a Tescan VEGA TS 5136XM equipped with an EDAX GENESIS 4000XMS EDS system. Spot analyses were acquired at 20 kV on specific microstructures evidenced in BSE images. The standardless method and the *ZAF* correction method were used for semi-quantitative analysis. Ion milling was performed with a Gatan precision ion polishing system (PIPS) instrument at the Earth Science Department of the University of Milan. The accelerating voltage was 5 kV during the first step of milling, then lower down to 2 kV for the finishing step. Transmission electron microscopy (TEM) investigations were performed at the Department of Physical Sciences, Earth and Environment of the University of Siena with a Jeol JEM 2010 instrument operating at

https://doi.org/10.1180/minmag.2016.080.154 Published online by Cambridge University Press

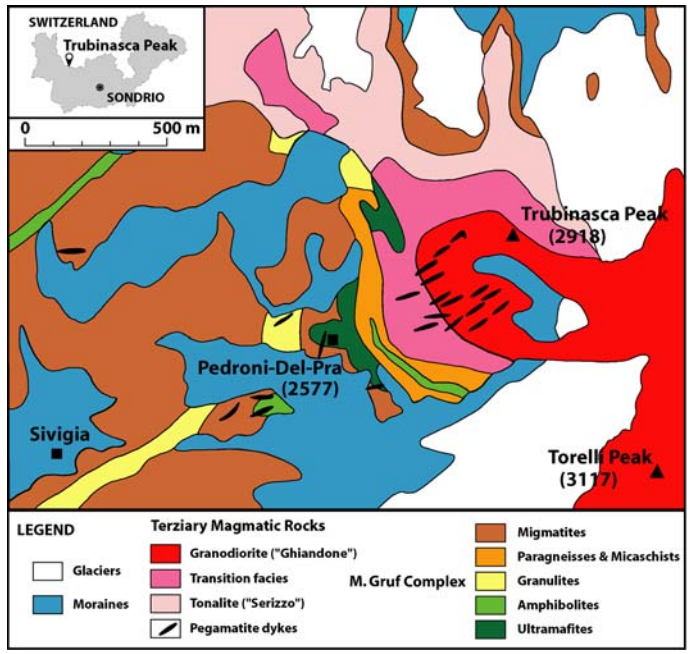

FIG. 2. Geolitological map of the upper Codera Valley (Sondrio, Italy) near Trubinasca Peak (from Bedogné *et al*. 1995, modified). The samples studied come from the closest dyke to the eastern side of the Pedroni-Del-Pra bivouac.

200 kV and equipped with an Oxford ISIS EDS system. To assure conductivity, samples were carbon coated before observation. The standardless method and the Cliff-Lorimer approximation (Cliff and Lorimer, 1975) were employed for semi-quantitative analysis. Images were acquired either on Kodak SO-163 photographic films or with a slow scan Olympus Tengra CCD camera with 2k × 2k resolution and 14 bit depth.

Results

Microstructure, mineral association and compositions (SEM-EDS results)

Back-scattered electron images of the polished samples reveal that they are aggregates of different phases. At least three different phases can be recognized in the low magnification image of Fig. 3. Higher magnification images of these different regions and EDS microanalyses reveal peculiar microstructures and distinct compositions. The wider area characterized by a dark grey BSE contrast in Fig. 3*a* is reproduced at higher magnification in Fig. 3*b*. The magnified image shows bean-shaped precipitates, <5 μm wide and 10 μm long, all parallel to a common elongation direction, embedded in a darker host. This suggests a crystallographic control of the host over the precipitates. Another kind of precipitate (indicated by small white arrows in Fig. 3*b*) are also observed in this region, characterized by a brighter contrast, needle-like habit, dimensions up to 5 μm long and ~1 μm wide, and with elongations along three distinct directions, according to a distorted hexagonal network. Crystallographic control in this case is also evident for the host, but whereas in the latter case threefold symmetry seems to act over the precipitates, in the former case the crystallographic control is only along one direction.

As expected from the different BSE contrast, host and precipitates are also distinguished by different chemical compositions. Representative SEM-EDS chemical analyses for these three different phases are reported in Table 1 for the two mounts (Meta 1 and Meta 2) prepared from the same hand specimen. The host and the bean shaped precipitates differ by the relative abundances of Ti, Mn and Fe. The composition of the host calculated for the Meta 1 sample on the basis of three oxygens (and discarding Nb and Ta, very close to the detection limit at 2 sigma level of confidence) gives

https://doi.org/10.1180/minmag.2016.080.154 Published online by Cambridge University Press

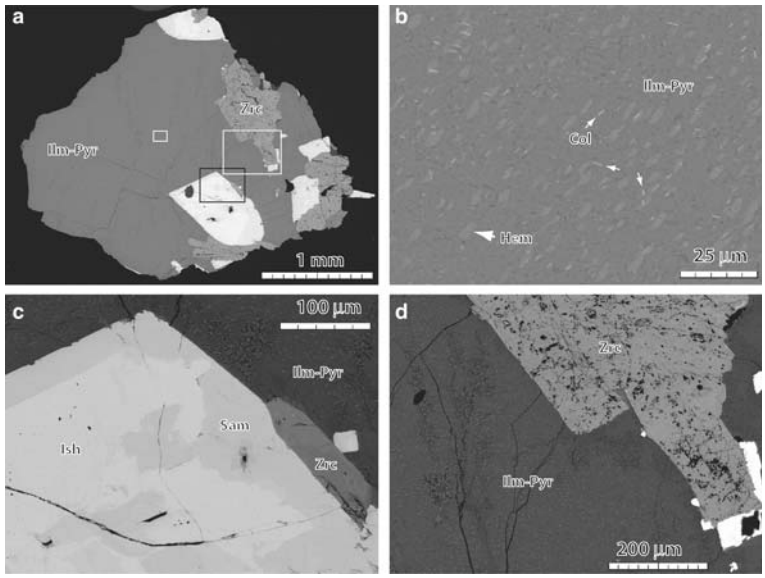

FIG. 3. SEM-BSE images of a polished section of sample 2. Sample 1 shows analogous microstructures with similar compositions. (*a*) Low magnification image showing the sample embedded in epoxy (peripheral dark contrast). At least three different phases can be recognized on the basis of the BSE contrast. (*b*) Magnification of the area enclosed in the white, small rectangle in (*a*) at the centre of the sample. Bean-shaped precipitates all parallel to a common direction (large arrow, 'Hem') and smaller, needle-like precipitates with elongation parallel to three directions according to a distorted hexagonal network (small arrows, 'Col') are embedded within a darker host ('Ilm-Pyr'). (*c*) High-magnification image of the area delimited by the dark rectangle in (*a*), which correspond to a zoned U-bearing phase compositionally consistent with samarskite-(Y) (dark grey, 'Sam') and ishikawaite (bright grey, 'Ish'). (*d*) High-magnification image of the area delimited by the white, large rectangle in (*a*). The brighter region, which is also detected at the top, at the bottom, and to the right of the sample in (*a*), is Hf-bearing zircon, and the irregular aspect of the surface is due, at least in part, to quartz inclusions.

$(Ti_{0.97}Fe_{0.57}Mn_{0.49})_{\Sigma=2.03}O_3$, which is consistent with an ilmenite–pyrophanite solid solution. The ilmenite–pyrophanite host in the Meta 2 sample shows a similar composition, but a slightly higher Fe/Mn ratio. The slightly higher cation totals in both samples, instead, may be due to a hematite component in solid solution. Following Carmichael (1967), the hematite component may be estimated by combining the bivalent elements Fe and Mn to Ti in the ratio 1:1 to form ilmenite and pyrophanite, and the exceeding iron considered as Fe^{3+} and allotted to form hematite. In this way, the Meta 1 host average composition can be expressed as $Pyr_{48}Ilm_{47}Hem_5$, and that of the Meta 2 sample $Ilm_{51}Pyr_{43}Hem_6$.

The chemical composition of the bean-shaped precipitates shows a much higher Fe/Mn ratio and lower Ti content with respect to the host, and could not be straightforwardly attributed to any simple mineral phase on the basis of the SEM-EDS results alone. Selected area electron diffraction (SAED) patterns, however, revealed a structure consistent with hematite (see below). Thus, assuming iron as Fe^{3+}, the composition is consistent with a Ti-rich hematite (or titanohematite) and expressed on the basis of six oxygens and discarding Nb and Ta, the average composition of the bean-shaped precipitates in the Meta 1 sample is $(Fe_{1.49}Ti_{0.33}Mn_{0.10})_{\Sigma=1.93}O_3$ (those of the Meta 2 sample shows a significant lower Fe/(Ti+Mn) ratio, Table 1). The lower cation total with respect to the ideal chemical formula may be due either to the presence of the heterovalent substitution $3Ti^{4+} + \square \leftrightarrows 4Fe^{3+}$, to ilmenite substitution in hematite, $Ti^{4+} + Fe^{2+} \leftrightarrows 2Fe^{3+}$, or to the presence of oxidized Mn^{3+}. The former entails the presence of 0.11 vacant sites per formula unit (pfu), which is higher than the observed cation deficiency. On the other hand, the latter two mechanisms would recast the total cations at somewhat higher, but still low, values.

https://doi.org/10.1180/minmag.2016.080.154 Published online by Cambridge University Press

TABLE 1. Semiquantitative SEM-EDS analyses of the non-metamict phases detected in the Codera-dyke samples. Each analysis refers to the average of 5–6 analytical spots.

	Meta 1						Meta 2					
Wt.%	Host	Range	Beans	Range	Needles	Range	Host	Range	Beans	Range	Needles	Range
Sc_2O_3					2.47	1.56– 3.08					1.18	0.96–1.47
TiO_2	49.45	48.96–49.88	17.04	14.12–21.01	20.92	14.06–31.55	49.10	47.88–49.60	22.33	20.66–24.74	28.35	22.07–33.51
MnO	22.22	20.48–26.87	4.71	3.07–6.97	9.27	5.67–15.51	19.99	19.54–20.19	7.28	6.50–8.25	13.05	5.41–17.15
FeO	26.33	21.36–28.96			21.16	17.06–33.28	29.05	28.52–30.60			28.45	20.97–36.32
Fe_2O_3			76.28	69.93–81.75					67.92	66.11–71.42		
Nb_2O_5	1.07	0.84–1.24	1.09	0.52–2.13	27.65	21.05–33.38	1.05	0.92–1.12	1.55	0.39–3.15	18.46	15.36–21.60
SnO_2					2.03	1.09–3.29					0.91	0.67–1.10
Ta_2O_5	0.93	0.62–1.16	0.87	0.54–1.45	16.51	11.55–19.69	0.82	0.50–1.06	0.93	0.32–1.72	9.61	7.76–11.77
Atoms per formula unit*												
Sc					0.12	0.07–0.16					0.06	0.05–0.07
Ti	0.95	0.95–0.96	0.33	0.27–0.40	0.90	0.64–1.29	0.95	0.93–0.96	0.42	0.39–0.47	1.19	0.97–1.37
Mn	0.48	0.45–0.58	0.10	0.07–0.15	0.45	0.29–0.72	0.43	0.43–0.44	0.16	0.14–0.18	0.61	0.26–0.80
Fe	0.56	0.46–0.62	1.47	1.33–1.58	1.02	0.81–1.68	0.62	0.61–0.66	1.29	1.25–1.36	1.34	0.96–1.77
Nb	0.01	0.01–0.01	0.01	0.01–0.02	0.72	0.52–0.88	0.01	0.01–0.01	0.02	0.00–0.04	0.47	0.38–0.56
Sn					0.05	0.02–0.08					0.02	0.01–0.03
Ta	0.01	0.00–0.01	0.01	0.00–0.01	0.26	0.17–0.31	0.01	0.00–0.01	0.01	0.00–0.01	0.15	0.12–0.18
Σ_{Cat}	2.02	2.01–2.03	1.91	1.90–1.92	3.52	3.41–3.78	2.02	2.02–2.04	1.89	1.88–1.91	3.84	3.67–4.01

*Atoms per formula unit (apfu) are on the basis of 3 oxygens for the ilmenite–pyrophanite host and for hematite (beans), and 6 oxygens for the columbite–tantalite needles. The latter does not fulfil the expected columbite stoichiometry because of the contamination from the host.

Assuming that the dominant mechanism is the ilmenite–pyrophanite substitution, as for most reported cases, the average composition of the bean-shaped precipitates in the Meta 1 sample can be expressed as $Hem_{65}Ilm_{24}Pyr_{11}$, and that of the Meta 2 sample $Hem_{55}Ilm_{29}Pyr_{17}$. In comparison with the host and bean-shaped precipitates, the needle-shaped precipitates show different proportions of Fe, Ti and Mn, significant amounts of Nb and Ta, and detectable amounts of Sc and Sn. However, because of the very small dimensions of the needles, contribution from the surrounding matrix to the SEM-EDS chemical analyses is certain. The identification of this phase was thus possible only using TEM (see below). Electron diffraction patterns and TEM-EDS analyses revealed a Ti-rich, Sc-bearing columbite phase. Because of the contribution from the surrounding, the SEM-EDS chemical analyses of the needles do not fit the expected columbite stoichiometry, and should be considered only qualitative.

The mineral association of the investigated samples is completed by a zoned U-bearing phase (Fig. 3*c*) and a U-free phase (Fig. 3*d*). The U-bearing phase shows varying U abundances with respect to other cations, and is responsible for the different BSE contrast. The simplified compositions that could be derived from SEM-EDS analyses are consistent with samarskite-(Y) (the dark grey regions), and ishikawaite (the brighter regions), and recalculation on the basis of four oxygens gives $[(Y_{0.22}U_{0.15}Dy_{0.04}Fe_{0.37}Mn_{0.03})_{\Sigma=0.81}(Nb_{0.76}Ta_{0.29}Ti_{0.14})_{\Sigma=1.19}O_4]$ and $[(U_{0.26}Y_{0.12}Dy_{0.04}Fe_{0.34}Mn_{0.08})_{\Sigma=0.84}(Nb_{0.76}Ta_{0.25}Ti_{0.14})_{\Sigma=1.16}O_4]$, respectively. It should be noted that there is a significant excess of B cations and a deficit of A cations with respect to the ideal formula, which, on the other hand, fits perfectly to the M:O = 1:2 stoichiometry. In order to understand the reasons for the observed discrepancy, the structural state of the U-bearing phases *versus* composition was investigated by TEM and reported elsewhere (Capitani *et al.*, 2016). The U-free, intermediate grey phase in the BSE image of Fig. 3*a* and shown at higher magnification in Fig. 3*d* has a chemical composition consistent with a Hf-bearing zircon, which recalculated on the basis of 4 oxygen atoms gives $(Zr_{0.90}Hf_{0.07}Si_{1.04})O_4$. The zircon shows a very irregular surface, presence of fractures and inclusions that the subsequent TEM investigation revealed to be quartz. The latter may be responsible of the slight Si excess found by microanalysis.

Structure relationships in the ilmenite–pyrophanite host (TEM-EDS and SAED results)

The bean-shaped precipitates within the ilmenite–pyrophanite host where recognized in TEM-EDS by their chemical composition and studied by selected area electron diffraction (SAED). The chemical composition measured by TEM-EDS for the ilmenite–pyrophanite host is consistent, within experimental error, with that obtained with SEM-EDS in the bulk sample. A significantly higher Fe/(Ti + Mn) ratio was detected in the titanohematite phase, which could be at least in part real and due to chemical zoning. Moreover, a low cation total was found in hematite, as in the bulk samples (Table 2). It should be noted that Nb and Ta, although always very close to the detection limit, are significant at the two sigma level in ilmenite–pyrophanite, whereas they are below the detection limit in titanohematite. SAED patterns confirm that the host has the ilmenite $R\bar{3}$ structure and the bean-shaped precipitates have the hematite $R\bar{3}c$ structure. The two structures are distinct in ⟨100⟩ SAED patterns because of the different space groups. The common $R\bar{3}$ lattice determines for both structures the presence of $-h + k + l = 3n$ reflections only, but in hematite, because of the *c* glide, only 0*kl* reflections with *l* even are present (Fig. 4). The two structures, however, exhibit identical SAED patterns when rotated ~30° around **c***, that is to say when observed down ⟨$\bar{1}$10⟩ (Fig. 5). From the SAED patterns we observe that ilmenite–pyrophanite and Ti-rich hematite have exactly the same orientation, suggesting that hematite exsolved from the host ilmenite–pyrophanite on cooling under more oxidizing conditions.

According to the TEM results, the needle-shaped precipitates have a structure consistent with a columbite phase. The higher spatial resolution of the TEM-EDS microanalysis with respect to SEM-EDS allowed the obtainment of the chemical composition without the interference of the ilmenite–pyrophanite and hematite host phases, which calculated on the basis of 6 oxygens reads $(Fe_{0.58}Sc_{0.25}Mn_{0.24}Sn_{0.11})_{\Sigma=1.18}(Nb_{1.25}Ti_{0.36}Ta_{0.30})_{\Sigma=1.91}O_6$, which can be defined as a Sc-bearing, Ti-rich columbite-(Fe)-tantalite-(Fe) mixture. This chemical formula, however, shows a high cation total with an excess of A cations paralleled by a deficiency of B cations. If part of the iron is presumed to be oxidized and occupying the B site, which is reasonable considering the presence of hematite, this inconsistency disappears. As previously inferred from SEM-BSE images, the

https://doi.org/10.1180/minmag.2016.080.154 Published online by Cambridge University Press

TABLE 2. TEM-EDS semi-quantitative chemical analyses for ilmenite–pyrophanite, hematite and columbite–tantalite (Meta 1 sample). Each column represents the average of 7, 7 and 3 spot analyses.

	Ilmenite–pyrophanite (host)		Titanohematite (beans)		Columbite–tantalite (needles)	
Wt.%	Mean	Range	Mean	Range	Mean	Range
Sc_2O_3					4.89	3.54–5.61
TiO_2	51.96	50.41–53.98	7.72	6.86–8.86	8.23	7.86–8.86
MnO	21.47	19.93–23.73	0.63	0.52–0.71	4.79	4.09–5.62
FeO	24.60	21.75–26.94			11.82	10.18–12.87
Fe_2O_3			90.92	89.95–92.06		
Nb_2O_5	0.78	0.00–1.20	0.21	0.00–0.38	47.01	43.04–52.49
SnO_2					4.59	3.07–5.59
Ta_2O_5	1.18	0.54–2.35	0.52	0.20–0.84	18.67	17.13–21.41
Atoms per formula unit*						
Sc					0.25	0.18–0.29
Ti	0.99	0.97–1.02	0.15	0.13–0.17	0.36	0.35–0.39
Mn	0.46	0.42–0.51	0.01	0.01–0.02	0.24	0.21–0.28
Fe	0.52	0.46–0.57	1.78	1.75–1.81	0.58	0.49–0.63
Nb	0.01	0.00–0.01	0.00	0.00–0.00	1.25	1.16–1.38
Sn					0.11	0.07–0.13
Ta	0.01	0.00–0.02	0.00	0.00–0.01	0.30	0.27–0.35
Σ_{Cat}	1.99	1.97–2.01	1.95	1.94–1.96	3.09	3.02–3.13

*Atoms pfu were recalculated on the basis of 3, 3 and 6 oxygens, respectively.

columbite phase has a crystallographic relationship with the ilmenite–pyrophanite host. From the SAED pattern of each phase, the following crystallographic orientation relationship can be established: $[100]_{Col}//[001]_{Ilm}$; $[001]_{Col}//\langle 110\rangle_{Ilm}$; $[010]_{Col}//\langle \bar{1}10\rangle_{Ilm}$ (Fig. 5).

Boundary interface in the exsolution microstructure (HRTEM results)

An area where ilmenite–pyrophanite (sometimes referred to as ilmenite in the following), titanohematite (sometimes just hematite) and columbite–tantalite (columbite) occur in contact is reported in the bright-field image of Fig. 6 (left). The three different phases were recognized by the different diffraction contrast and identified through EDS spectra (right). A high-resolution image of the ilmenite–hematite contact as viewed down $\langle 100\rangle$ is reported in Fig. 7. The boundary is crystallographically coherent, sharp, and occurs roughly parallel to (001). The two phases show different unit-cell dimensions, as testified by the spot separation in the related SAED pattern (top right) and in the Fast Fourier Transform (FFT) taken across the interface (lower right). This geometrical difference causes structural misfit and elastic strain at the hematite–ilmenite interface and is the cause of the strain contrast (dark bands) observed in the middle and top parts of the image (left). The HR images of Fig. 8 refer to ilmenite–columbite and hematite–columbite contacts as seen down $\langle \bar{1}10\rangle$ of ilmenite and hematite, which is parallel to [010] of columbite. The boundaries are crystallographically coherent, and develop roughly parallel to (100) of columbite and (001) of hematite and ilmenite. A geometrical misfit between the structures of rhombohedral phases and columbite is observed along this projection, and is especially evident at the hematite–columbite interface, where the FFTs taken across the interface show spot separation of high-order reflections. This geometrical misfit is possibly the cause of dislocation-like defects observed at the interface and the associated strain contrast. Spot separation is not visible in the FFT taken at the ilmenite–columbite interface. This observation should depose in favour of a better fit between the ilmenite and columbite structures along $\mathbf{a}_{Col}//\mathbf{c}_{Ilm}$ than between those of hematite and columbite. Lattice-fit calculations seem to confirm this hypothesis (see below). However, dislocation-like defects are observed also along

https://doi.org/10.1180/minmag.2016.080.154 Published online by Cambridge University Press

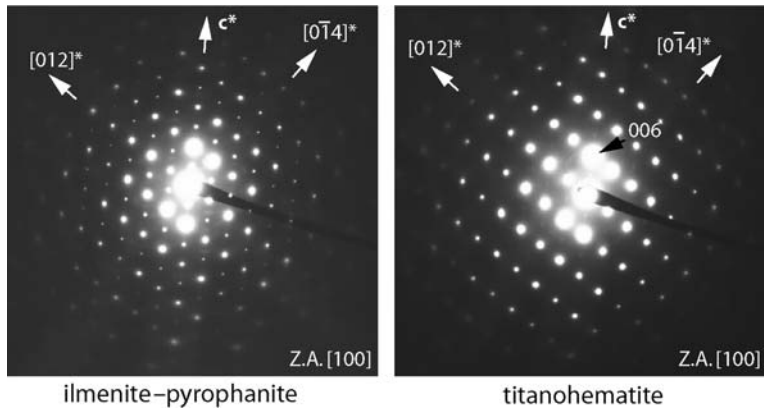

FIG. 4. SAED patterns showing the close structure similarities between the ilmenite–pyrophanite host and the exsolved titanohematite and their identical orientation (the tilt angles of the TEM goniometer were not moved on passing from one phase to the other).

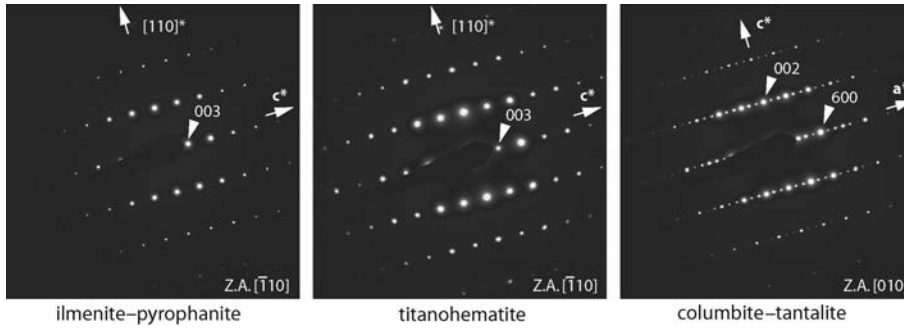

FIG. 5. SAED patterns of ilmenite–pyrophanite, hematite and columbite–tantalite. Note the orientation relationship between the rhombohedral phases and columbite.

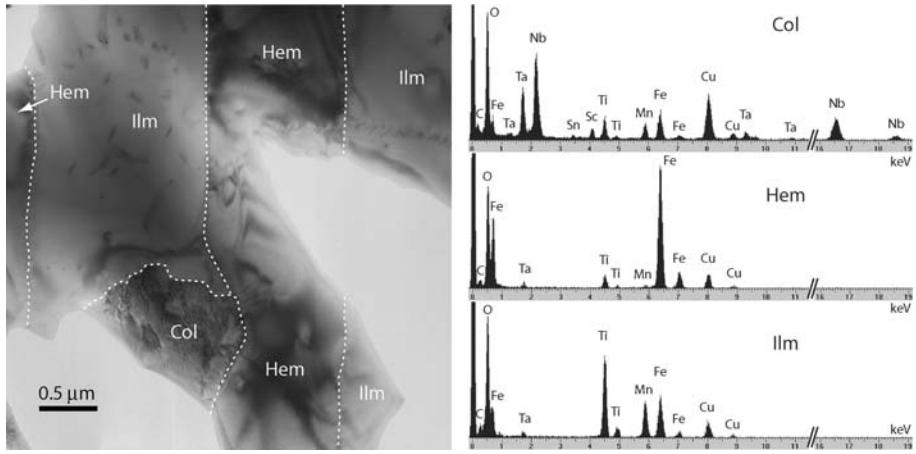

FIG. 6. Bright-field image of an area in which ilmenite–pyrophanite (Ilm), titanohematite (Hem) and columbite–tantalite (Col) are in contact (left). Each of them shows a clearly distinct EDS spectrum (right).

https://doi.org/10.1180/minmag.2016.080.154 Published online by Cambridge University Press

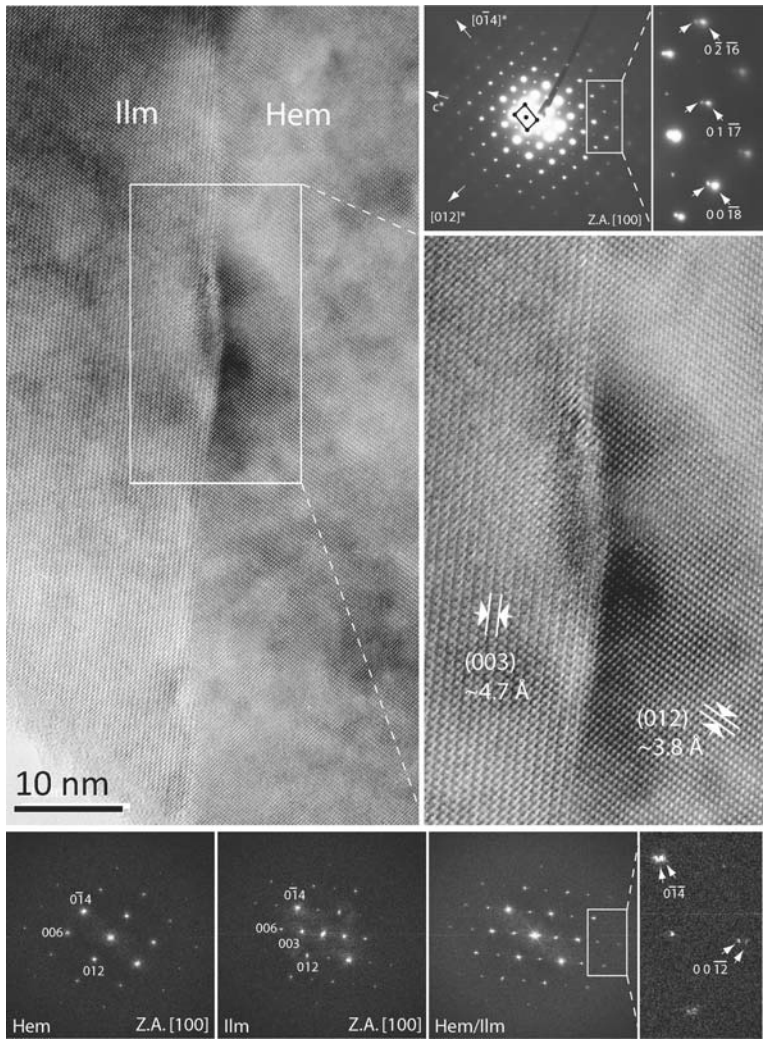

FIG. 7. HR image of the ilmenite–hematite boundary as seen down [100] (left) and related SAED pattern (upper right). The enlarged view of the HR image shows an offset along the contact running parallel to (001), associated to lattice strain (dark). Lower row, from left to right: FFTs of free hematite (Hem), ilmenite (Ilm), and of the Hem/Ilm interface. Note the spot separation affecting the latter, indicating a slightly different repeat unit along [001].

this contact. From the above HR images, the structural relationship $\mathbf{c}_{Col}//\langle 110\rangle_{Ilm}$, $\mathbf{a}_{Col}//\mathbf{c}_{Ilm}$ and $\mathbf{b}_{Col}//\langle \bar{1}10\rangle_{Ilm}$, is inferred. Exsolution microstructures were also found at a finer scale. Figure 9 shows nanometre-sized columbite lamellae within hematite. Columbite lamellae are elongated along **c** and their (100) planes form coherent contacts with the (001) lattice planes of hematite. Coherent but shorter and irregular contacts develop at high angles with this direction. However, neither pervasive nanosized exsolution lamellae of hematite within ilmenite, nor nanosized ilmenite within hematite were observed in these samples.

Discussion

The results from TEM and SEM identified unambiguously an ilmenite–pyrophanite s.s. host with titanohematite and columbite–tantalite s.s.

https://doi.org/10.1180/minmag.2016.080.154 Published online by Cambridge University Press

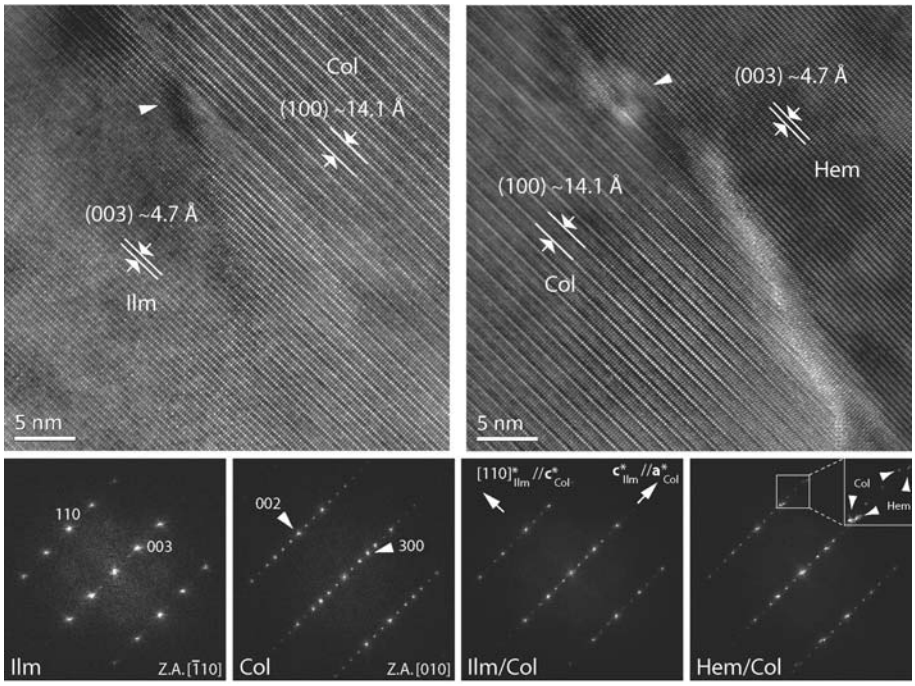

FIG. 8. HR image of the ilmenite–columbite contact (upper left) and hematite–columbite contact (upper right) as seen down $\langle\bar{1}10\rangle$ of ilmenite and hematite, which is parallel to [010] of columbite. Note the dislocation-like contrast at boundary interfaces (arrows). Lower row, from left to right: FFT of free ilmenite (Ilm), indistinguishable from that of hematite along this projection as the 00*l* reflections, which should be absent for $l \neq 2n$ because of the *c* glide, are indeed present because of dynamic effects – columbite (Col), ilmenite/columbite (Ilm/Col) and hematite/columbite (Hem/Col) contacts. Spot separations are observed in the latter (arrows).

precipitates, and showed their crystallographic orientation relationships. The fact that the rhombohedral phases form extended solid solution at high temperature (Gaspar and Wyllie 1983; Zaccarini *et al.*, 2004), suggests that titanohematite and columbite formed through exsolution from an ilmenite–pyrophanite host, and that the observed microstructure represents a solvus microstructure produced during cooling or induced by oxidation reactions. From a textural point of view, the temporal sequence of exsolution cannot be simply assessed. Columbite forms both in titanohematite lamellae and in the ilmenite–pyrophanite host, and in some cases a single columbite grain crosscuts the hematite–ilmenite boundary. We believe that if columbite exsolved first, hematite could not grow into continuous crystals as are showed by SEM, as the already formed columbite crystals would have represented an obstacle to diffusion, required for the growth of the hematite lamellae. Thus, the suggested sequence of exsolution is hematite first, followed by columbite.

Titanohematite exsolutions in ilmenite–pyrophanite

Exsolution microstructures in the $FeO–Fe_2O_3–MnO–TiO_2$ system seem a common feature and may occur at a microscopic scale (Haggerty, 1991) as well as at a nanometre scale (e.g. Kasama *et al.*, 2003, 2004). This complex system has been studied experimentally by Mazzullo *et al*. (1975) at 1 kbar and 700–1000°C. In this *P–T* range, Mn-bearing ulvöspinel–magnetite solid solution and ilmenite–hematite solid solution coexist, with MnO partitioning preferentially into ilmenite. The same is observed in the samples from the Codera dyke pegmatite (Table 1), consistently with the presumed similar geochemical behaviour of Mn^{2+} and Fe^{2+}. Many more studies focus on the ternary $FeO–Fe_2O_3–TiO_2$ system. In particular, the ilmenite–hematite solid solution has been investigated experimentally by a number of studies (Lindsley, 1991). All these studies were hampered by very

https://doi.org/10.1180/minmag.2016.080.154 Published online by Cambridge University Press

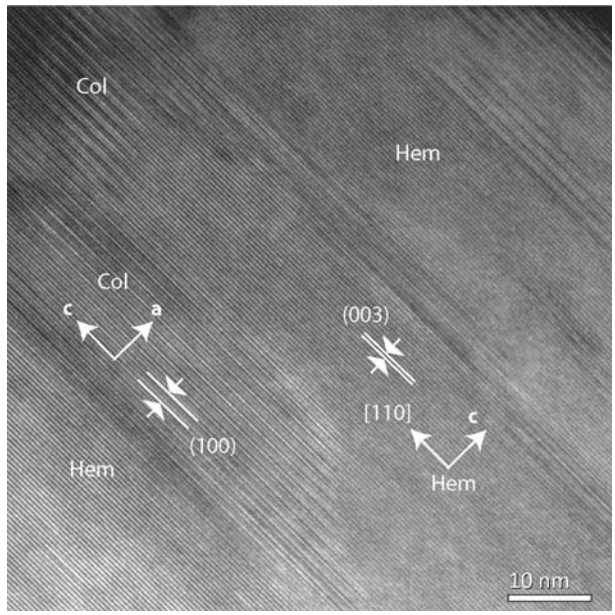

FIG. 9. Lattice fringe image showing columbite lamellar exsolutions (Col) within hematite (Hem) (electron beam incidence $\langle \bar{1}10 \rangle_{Hem} // [010]_{Col}$). Columbite exsolutions are recognized promptly by their higher (001) interplanar distance (~14.1 Å) as compared by the three times smaller interplanar distance of hematite (003) planes (~4.7 Å).

slow chemical reaction rates, but they succeeded in showing that the consolute point lays below 650°C and is strongly asymmetrical towards hematite. A miscibility gap was then encountered along the ilmenite–hematite join at 600°C at 1–2 kbar. Comphrensive 1-atm *T–X* phase diagrams combining experimental and theoretical aspects are by Burton (1991) and Harrison and Becker (2001) (Fig. 10). The most significant difference is the location of the eutectoid temperature, placed at 520°C in Burton (1991), and at the much lower temperature of 390°C in Harrison and Becker (2001). Bulk compositions more Ti-rich than Ilm_{28} (Burton 1991) and Ilm_{31} (Harrison and Becker, 2001) are present above the eutectoid *T* as coexisting paramagnetic (PM) $R\bar{3}$ Ilm_{ss} and PM $R\bar{3}c$ Hem_{ss}. At the eutectoid *T*, PM $R\bar{3}$ Hem_{ss} breaks down on cooling to a two phase mixture of antiferromagnetically ordered (CAF) Hem_{ss} and PM $R\bar{3}$ Ilm_{ss}. Bulk compositions more Ti-rich than $Ilm_{83–85}$, like those observed in this study, above the eutectoid *T* are present only as a paramagnetic $R\bar{3}$ Ilm_{ss} single phase that, on cooling, should evolve into a two-phase mixture of antiferromagnetically ordered Hem_{ss} and $R\bar{3}$ Ilm_{ss}.

Assuming that Mn^{2+} behaves geochemically as Fe^{2+}, thus equating pyrophanite to ilmenite, the hosting phase detected in this study has an approximate composition $Ilm_{95}Hem_5$ (Meta 1) and $Ilm_{94}Hem_6$ (Meta 2) and the titanohematite precipitates $Ilm_{35}Hem_{65}$ and $Ilm_{45}Hem_{55}$, respectively. The related volume amounts of each phase estimated through particle analysis of BSE images like that in Fig. 3*b* are ~11.2% Hem_{65} in the Meta 1 sample and ~11.5% Hem_{55} in the Meta 2 sample (the amounts of columbite are ~1.2% and ~1.0%, respectively). As hematite and ilmenite have very similar molar volumes, volume per cent and moles per cent can be compared directly and used to calculate the bulk compositions before exsolution, which result in $Ilm_{88}Hem_{12}$ for sample Meta 1 and $Ilm_{89}Hem_{11}$ for sample Meta 2 (Table 3). The compositions of the bulk ilmenite–pyrophanite before exsolution and of the ilmenite–pyrophanite host and titanohematite precipitates are reported as vertical lines in the *T–X* phase diagrams of Burton (1991) and Harrison and Becker (2001). It should be noted that these compositions do not reasonably plot on these diagrams assuming equilibrium conditions, because the ilmenite-rich host should be in equilibrium with precipitates much richer in hematite. Even accounting for any inaccuracy of the analytical method, possible inaccuracy in the phase diagrams, and errors in the particle analysis, the

https://doi.org/10.1180/minmag.2016.080.154 Published online by Cambridge University Press

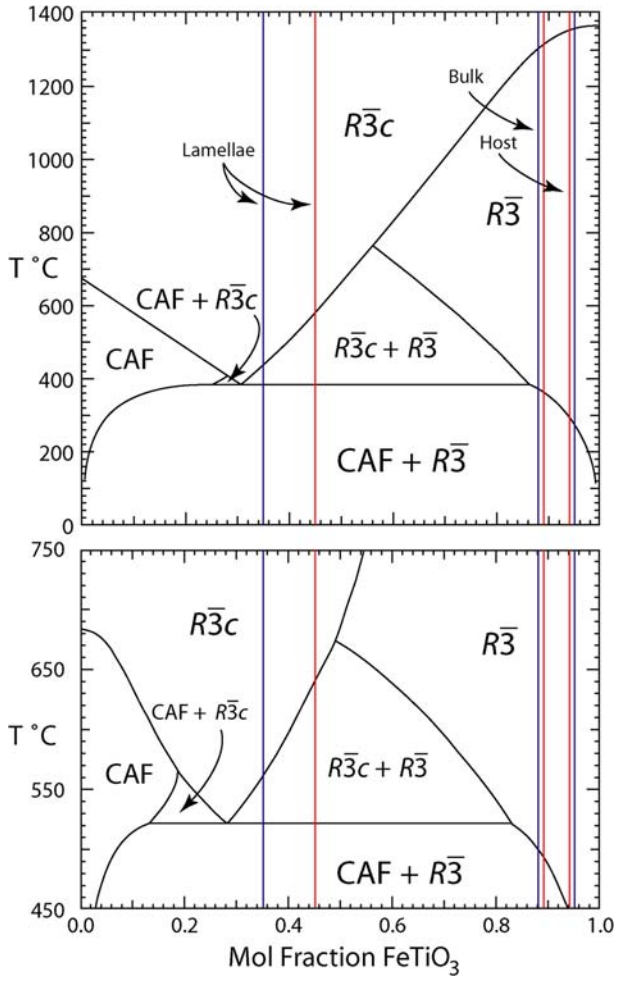

FIG. 10. *T–X* phase diagrams for the Fe_2O_3–$FeTiO_3$ system, modified from Burton (1991) and Harrison and Becker (2001). Vertical lines represent chemical compositions of the bulk ilmenite–pyrophanite before exsolution and of the ilmenite–pyrophanite host and of the titanohematite precipitates after exsolution (blue = Meta 1 sample; red = Meta 2 sample).

observed discrepancy cannot be explained. Possible causes must be related either to metastability of the observed compositions, or effects of additional components such as $MnTiO_3$. We believed the latter is the likely cause of the observed discrepancy. Indeed, in spite of the similar geochemical and crystal-chemical behaviour of Mn and Fe in many geological processes (Capitani and Mellini, 2000*a*,*b*), the larger cation radius of Mn^{2+} (0.81 Å) substituting for Fe^{2+} (0.75 Å) in the ilmenite structure, a compact structure, can significantly affect the ideality of the solid solution (Evans *et al.*, 2006), and thus the size and extent of the ilmenite–hematite two phase field.

Columbite–tantalite exsolutions

Exsolution lamellae of mangano-columbite and hematite in primary manganoan ilmenite, very similar to those described here, were reported previously by Beurlen *et al.* (2006) from the Pitombeiras Pegmatite, Borborema Pegmatitic Province, Acarí County, Brazil. These authors described <2 μm × 30 μm exsolution lamellae forming hexagonal arrangements in pinacoidal sections of hosting ilmenite and, on the basis of the angle they formed with the (0001) hematite lamellae when observed in prismatic sections, they suggested $\{2hh\bar{3}hl\}$ as the exsolution plane.

https://doi.org/10.1180/minmag.2016.080.154 Published online by Cambridge University Press

TABLE 3. End-member compositions of ilmenite–pyrophanite, titanohematite and columbite–tantalite from the Codera pegmatite along with their volume proportions, calculated cell parameters, and lattice misfit between columbite and hosts, along the three crystallographic axes of columbite.

	Meta 1			Meta 2		
	Ilm–Pyr	Ti-Hem	Col–Tan	Ilm–Pyr	Ti-Hem	Col–Tan
Ilm	0.47	0.24	–	0.51	0.29	–
Pyr	0.48	0.11	–	0.43	0.17	–
Hem	0.05	0.65	–	0.06	0.55	–
Col–(Fe)	–	–	0.56	–	–	0.50
Col–(Mn)	–	–	0.25	–	–	0.40
Tan-(Fe)	–	–	0.14	–	–	0.06
Tan-(Mn)	–	–	0.06	–	–	0.05
Vol.%	87.6	11.2	1.2	87.5	11.5	1.0
a(Å)	5.11	5.06	14.30	5.11	5.07	14.31
b	5.11	5.06	5.73	5.11	5.07	5.74
c	14.19	13.91	5.06	14.18	13.96	5.06
Δ_a%	0.80	2.70		0.93	2.48	
Δ_b%	2.99	1.99		2.83	2.02	
Δ_c%	1.06	0.07		1.02	0.22	

Actually, Beurlen *et al*. (2006) could not distinguish on the basis of the sole microprobe analyses if the precipitates were columbite or ixiolite, because of the partial compositional overlap of these two mineral groups. Here we present a more detailed description of columbite–tantalite precipitates in ilmenite–pyrophanite with exsolutions of titanohematite, of their boundary and their crystallographic relationships with the host. We found experimentally that $\mathbf{c}_{Col}//\langle 110\rangle_{Ilm}$, $\mathbf{a}_{Col}//\mathbf{c}_{Ilm}$, and $\mathbf{b}_{Col}//\langle \bar{1}10\rangle_{Ilm}$. This crystallographic relationship can be understood in terms of preservation of the oxygen close packing and thus of the parallelism between octahedral layers of the ilmenite host with those of the columbite precipitates (Figs 1*a* and *b*). The elongation of the needle-shaped columbite–tantalite crystals could be along [001], that is to say the direction of the octahedral chains in the columbite structure (Fig. 1*b* and *c*). Because of the presence the $\bar{3}$ axis perpendicular to the octahedral layers in the rhombohedral ilmenite structure, the columbite–tantalite precipitates may show [001] elongation direction parallel to any of the three equivalent ⟨110⟩ directions, explaining the hexagonal arrangement of columbite needles observed in SEM-BSE images. Actually, the measured interangles of the columbite needles in our BSE images deviates from 60° because the sample is cut significantly off the pinacoidal section. Indeed, the projection of a hexagon on an inclined plane is a distorted hexagon. For the same reason, the titanohematite precipitates, which have a discoidal shape flattened on (001), appear elliptical (bean-like), with the long axis normal to the dip of the actual section. It should be noted that this crystallographic relationship preserves the same crystallographic orientation of the octahedral chains in the columbite and ilmenite structures (Figs 1*c* and *d*). TEM observations on a few columbite crystals support this hypothesis (Fig. 11), which is also consistent with lattice-fit considerations, as explained below. Because cell parameters derived from SAED patterns may be inaccurate unless a dedicated camera length calibration and lens distortion correction is undertaken (Capitani *et al.*, 2006; Mugnaioli *et al.*, 2009; Mitchell, 2015), the cell parameters of ilmenite–pyrophanite were derived from the chemical composition detected with the SEM through linear regression analyses of the data on $FeTiO_3$–$MnTiO_3$ solid solutions (Wu *et al.*, 2010). The same approach was employed for estimating the cell parameters of the ilmenite–pyrophanite solid solution component within hematite, then the cell parameters of hematite were calculated by averaging these cell parameters and those of a pure hematite (Blake and Hessevick, 1966), taking into account their respective molar proportions. Finally, the cell parameters of the columbite–tantalite precipitates were estimated through the composition detected by TEM

https://doi.org/10.1180/minmag.2016.080.154 Published online by Cambridge University Press

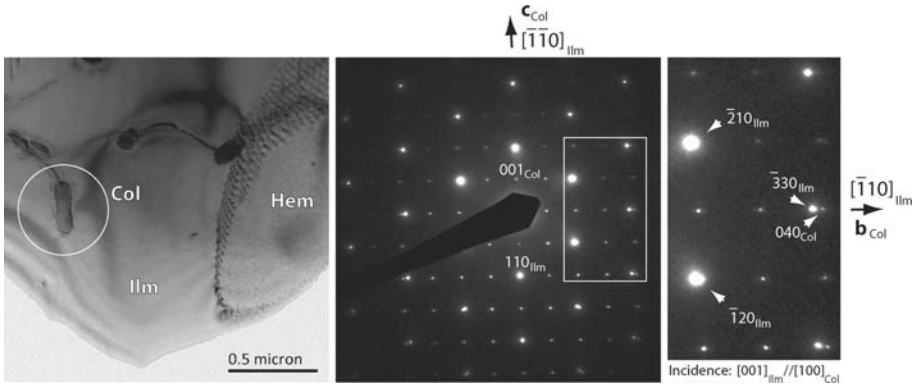

FIG. 11. Left: bright-field image of the Meta 2 sample showing a small columbite crystal (circled) embedded within ilmenite–pyrophanite (Ilm) in contact with titanohematite (Hem) to the right. The contact Ilm/Hem is approximately parallel to (001) and the observation direction slightly away from [001]. This makes the two phases partially overlap, giving rise to the observed hexagonal net contrast, which can thus be explained as a Moiré-like interference figure due to the slightly different cell parameters of ilmenite and hematite. Centre: SAED pattern referring to columbite and ilmenite (circled area in the left image) taken after the beam incidence was set parallel to $[001]_{Ilm}//[100]_{Col}$. Note the crystallographic relationship $[\bar{1}10]_{Ilm}//[010]_{Col}$ and $[\bar{1}\bar{1}0]_{Ilm}//[001]_{Col}$. The elongation direction of the columbite crystal is parallel to [001]. Right: enlargement of the reciprocal space pattern outlined on the previous image to emphasize the spot separation due the different cell dimensions of ilmenite and columbite. The calculated lattice misfit along $[010]_{Col}$ is 3.9% and that along $[001]_{Col}$ is 1.3%. These values are slightly higher than that calculated on the basis of the mineral composition, but their relative 3:1 ratio is preserved (Table 3).

applying the equation of Ercit *et al*. (1995). The results are reported in Table 3 along with the composition of the involved phases and the lattice misfit between columbite and host along their common orientation directions. The calculations take into account that along $\mathbf{b}_{Col}//\langle\bar{1}10\rangle_{Ilm}$, the columbite repeat unit encompasses two octahedral strips, but only 1.5 that of ilmenite. Overall, from these data it is evident that a minimal lattice misfit exists along the common direction $\mathbf{c}_{Col}//\langle 110\rangle_{Ilm}$. Thus it is reasonable that to minimize elastic strain at the interface with the host, columbite needles grow faster along **c**, minimizing the *ab* surface. It should be noted, however, that a direction of minimal lattice misfit exists also along $\mathbf{a}_{Col}//\mathbf{c}_{Ilm}$, suggesting that columbite precipitates could grow as lamellae instead of needles in the ilmenite–pyrophanite host. SEM images taken on sample sections cut close to the ilmenite prism section, however, show equant columbite grains, thus denying this hypothesis.

Nb and Ta solubility in ilmenite–pyrophanite

The Nb and Ta content of ilmenite–pyrophanite solid solutions has received, so far, marginal attention in the literature. Garanin *et al*. (1980) used the average abundance of Nb_2O_5 and Ta_2O_5 to distinguish ilmenites of carbonatites (1.11 and 0.13 wt.%, respectively) from those of kimberlites (0.22 and 0.16 wt.%, respectively) in Russian rocks from several localities. Gaspar and Wyllie (1983) reported ilmenites from the Jacupiranga carbonatites with ($Nb_2O_5 + Ta_2O_5$) content up to 3.68 wt.% that inversely correlated with the age of the intrusion, consistently with the geochemical concentration of incompatible elements in liquids during differentiation. The amount of ($Nb_2O_5 + Ta_2O_5$) of the ilmenite–pyrophanite forming the Codera pegmatite before exsolution of hematite and columbite, estimated on the basis of TEM-EDS analyses and of the volume fraction of each exsolved phase, is ~2.8 wt.%. This small amount would suggest a small solubility, at low temperature, of Nb and Ta in the ilmenite structure. The highest (Nb + Ta) content observed in natural ilmenites has been reported for hypabyssal calcite kimberlite from the Internatsional'naya intrusion in Yakutia, Russia. Here, manganoan niobian ilmenite containing up to 9.5 wt.% MnO, 12.5 wt.% Nb_2O_5 and 0.8 wt.% Ta_2O_5 were described (Chakhmouradian and Mitchell, 1999). The exceptionally high Nb content probably reflects a high-

https://doi.org/10.1180/minmag.2016.080.154 Published online by Cambridge University Press

temperature mineral composition, considering the fast cooling rate of this peculiar petrogenetic environment. Other known occurrences of niobian ilmenite from petrogenetic environments with cooling rates comparable with that expected for the Codera dyke suite include ultramafic lamprophyre dykes in West Greenland (Mitchell *et al.*, 1999) and a granitic pegmatite at Prašivá, Slovakia (Uher *et al.*, 1998). These rocks contain ilmenites with Nb_2O_5 up to 6.7 and 7.2 wt.%, respectively, higher than those observed in this study and also higher than the maximum contents of 4.0 wt.% $Nb_2O_5 + Ta_2O_5$ in pegmatitic ilmenite referred to by Černý and Ercit (1989). A possible cause of the observed difference may be the high MnO content of the Codera-dyke ilmenite, which is suggested here to lower the Nb + Ta solubility at low temperatures. As the Garnet Codera pegmatite is supposed to be emplaced during a syn-magmatic stage above 500°C (Guastoni *et al.*, 2014), assuming that the exsolution process initiated during cooling after emplacement, a wide solvus in the exotic system $FeMnTi_2O_6$–$FeNbTaO_6$ is expected below 500°C.

Conclusions

In this paper we report exsolutions of titanohematite and columbite–tantalite in ilmenite–pyrophanite crystals from the Garnet Codera dyke pegmatite (Italian Alps). The titanohematite precipitates share the same crystallographic orientation of the ilmenite–pyrophanite host and show a discoidal shape parallel to (001), alike many other reported cases. In contrast, although columbite in association with ilmenite-group minerals is not infrequent in granitic pegmatites, columbite exsolution in ilmenite–hematite is a rarely documented phenomenon. As far as we know, this is the second report of this kind, the other one being the report of Beurlen *et al*. (2006), although these authors could not definitely establish if the exsolved phase was columbite or ixiolite. Other claimed columbite exsolutions in ilmenite–hematite phase actually are, at least judging from the microstructure, secondary depositions within cracks or voids of the host phase rather than real exsolutions (ie. Hirtopanu *et al.*, 2015). In this work, for the first time, a detailed description of columbite–tantalite microscopic and submicroscopic precipitates in ilmenite–pyrophanite solid solution with lamellae of titanohematite is reported, their crystallographic relationships determined, and their contact interfaces described. The columbite–tantalite precipitates form a hexagonal network of needles elongated along ⟨110⟩ of the ilmenite–pyrophanite host, with coherent contacts. The following crystallographic relationship was established: $[100]_{Col}//[001]_{Ilm}$; $[001]_{Col}//\langle 110\rangle_{Ilm}$; $[010]_{Col}//\langle \bar{1}10\rangle_{Ilm}$. On the basis of textural observation, titanohematite is supposed to exsolve first, followed by columbite–tantalite at a temperature below 500°C. The amount of $(Nb_2O_5 + Ta_2O_5)$ of the ilmenite–pyrophanite forming the Codera pegmatite before exsolution has been estimated to be ~2.76 wt.%. This is lower than levels reported for other occurrences where exsolution microstructures were not observed. Whereas in some cases the lack of exsolutions can be explained by the fast cooling rate that quenched the high-temperature state (Chakhmouradian and Mitchell, 1999), in other cases, with cooling rates comparable to that expected for the Codera pegmatite, the above cannot be a valid explanation. We note the cases of ultramafic lamprophyre dykes in West Greenland, with Nb_2O_5 up to 6.7 wt.% (Mitchell *et al.*, 1999) and that of the granitic pegmatite at Prašivá, Slovakia, with Nb_2O_5 up to 7.2 wt.% (Uher *et al.*, 1998). In the present work it is suggested that significant addition of MnO could lower the Nb + Ta solubility in ilmenite at low temperatures. If this were the case, a wide solvus in the exotic system $FeMnTi_2O_6$–$FeNbTaO_6$ is expected below 500°C. The compositions of the bulk ilmenite–pyrophanite before exsolution and those of the ilmenite–pyrophanite host and titanohematite precipitates do not correctly plot on *T–X* phase diagrams of Burton (1991) and Harrison and Becker (2001), assuming equilibrium conditions. The possible cause has been indicated in the effects that an additional component, namely $MnTiO_3$, could have on the phase diagram topology. Actually, the present data would correctly plot on the phase diagrams if the low-temperature two-phase field is contracted to the ilmenite side, i.e. allowing more ilmenite component to enter the hematite structure. This observation implies the need of further investigations on the effects of a non-binary component in the Fe_2O_3–$FeTiO_3$ system. We did not find a dense distribution of nanometric exsolutions, potential carriers of lamellar magnetism in the ilmenite–pyrophanite from the Garnet Codera dyke, as has been the case in other contexts (McEnroe *et al.*, 2001, 2002). On the other hand, the contact layer composition at the columbite–ilmenite and columbite–hematite interfaces is not known, but any magnetic property

https://doi.org/10.1180/minmag.2016.080.154 Published online by Cambridge University Press

carried by each single needle is probably neutralized by the almost isotropic distribution (actually hexagonal) of the columbite needles on the (001) plane of ilmenite. For these reasons, the remanent magnetization is expected to be low in these samples.

Acknowledgements

Alessandro Guastoni is acknowledged for providing the Garnet Codera dyke samples. Matteo Sala collaborated in preparing the samples for SEM and TEM observations. Paolo Gentile is acknowledged for assistance with the SEM. This paper has benefited from comments by Federica Zaccarini and one anonymous referee.

References

Bedogné, F., Maurizio, R., Montrasio, A. and Sciesa, E. (1995) *I Minerali della Provincia di Sondrio e della Bregaglia Grigionese: Val Bregaglia, Val Masino, Val Codera e Valle Spluga*. Bettini, Sondrio, p. 300.

Beurlen, H., Thomas, R., Da Silva, M.R.R. and Silva, D. (2006) Manganocolumbite and cassiterite exsolution lamellae in ilmenite from the Pitombeiras pegmatite (Acari – Rio Grande do Norte) in the Borborema Pegmatitic Province, NE-Brazil. *Estudos Geológicos*, **16**, 3–15.

Blake, R.L. and Hessevick, R.E. (1966) Refinement of the hematite structure. *American Mineralogist*, **51**, 123–129.

Burton, B.P. (1991) The interplay of chemical and magnetic ordering. Pp. 303–321: *Oxide Minerals: Petrologic and Magnetic Significance* (D.H. Lindsley, editor). Reviews of Mineralogy, **25**. Mineralogical Society of America, Washington, DC.

Capitani, G.C. and Mellini, M. (2000*a*) The crystallisation sequence of the Campiglia M.ma skarn (Livorno, central Italy). *Neues Jahrbuch für Mineralogie Monatshefte*, **3**, 97–115.

Capitani, G.C. and Mellini, M. (2000*b*) The johannsenite–hedenbergite complete solid solution: clinopyroxenes from the Campiglia Marittima skarn. *European Journal of Mineralogy*, **12**, 1215–1227.

Capitani, G.C., Oleynikov, P., Hovmoeller, S. and Mellini, M. (2006) A practical method to detect and correct for lens distortion in the TEM. *Ultramicroscopy*, **106**, 66–74.

Capitani, G.C., Mugnaioli, M. and Guastoni, A. (2016) What is the actual structure of samarskite-(Y)? A TEM investigation of metamict samarskite from the Garnet Codera dyke pegmatite (Central Italian Alps). *American Mineralogist*, **101**, 1679–1690.

Carmichael, I.S.E. (1967) The iron-titanium oxides of silicic volcanic rocks and their associated ferromagnesian silicates. *Contributions to Mineralogy and Petrology*, **14**, 36–64.

Černý, P. and Ercit, T.S. (1989) Mineralogy of niobium and tantalum: crystal chemical relationships, paragenetic aspects and their implications. Pp. 27–79 in: *Lanthanides, Tantalum, Niobium: Mineralogy, Geochemistry, Characteristics of Primary Ore Deposits, Prospecting, Processing and Applications* (P. Moeller, P. Cerný and F. Saupé, editors). Springer, Heidelberg, Germany.

Chakhmouradian, A.R. and Mitchell, R.H (1999) Niobian ilmenite, hydroxylapatite, sulfatian monazite: alternative hosts for incompatible elements in calcite kimberlite from Internatsional'naya, Yakutia. *The Canadian Mineralogist*, **37**, 1177–1189.

Cliff, G. and Lorimer, G.W. (1975) The quantitative analysis of thin specimens. *Journal of Microscopy*, **103**, 203–207.

De Michele, V. and Zezza, U. (1979) Le pegmatiti dell'Alta Val Codera (Sondrio) nell'area di Punta Trubinasca. *Atti della Società italiana di scienze naturali e del Museo civico di storia naturale di Milano*, **120**, 180–194.

Ercit, T.S., Wise, M.A. and Černý, P. (1995) Compositional and structural systematics of the columbite group. *American Mineralogist*, **80**, 613–619.

Evans, B.W., Scaillet, B. and Kuehner, S.M. (2006) Experimental determination of coexisting iron-titanium oxides in the systems FeTiAlO, FeTiAlMgO, FeTiAlMnO, and FeTiAlMgMnO at 800 and 900°C, 1-4 kbar, and relatively high oxygen fugacity. *Contributions to Mineralogy and Petrology*, **152**, 149–167.

Garanin, V.K., Kudryavtseva, G.P. and Lapin, A.V. (1980) Typical features of ilmenite from kimberlites, alkali-ultrabasic intrusions, and carbonatites. *International Geology Review*, **21**, 1025–1050.

Gaspar, J.C. and Wyllie, P.J. (1983) Ilmenite (high Mg, Mn, Nb) in the carbonatites from the Jacupiranga Complex, Brazil. *American Mineralogist*, **68**, 960–971.

Guastoni, A., Pennacchioni, G., Pozzi, G., Fioretti, A.M. and Walter, J.M. (2014) Tertiary pegmatite dykes of the Central Alps. *The Canadian Mineralogist*, **52**, 641–669.

Lindsley, D.H. (1991) Experimental studies of oxide minerals. Pp. 69–106 in: *Oxide Minerals: Petrologic and Magnetic Significance* (D.H. Lindsley, editor). Reviews in Mineralogy, **25**. Mineralogical Society of America, Washington DC.

Haggerty, S.E. (1991) Oxide texture – a mini-atlas. Pp. 129–219 in: *Oxide Minerals: Petrologic and Magnetic Significance* (D.H. Lindsley, editor). Reviews in Mineralogy, **25**. Mineralogical Society of America, Washington DC.

Harrison, R.J. and Becker, U. (2001) Magnetic ordering in solid solutions. *European Mineralogical Union Notes in Mineralogy*, **3**, 349–383.

Hirtopanu, P., Fairhurst, R.J. and Jakab, G. (2015) Niobian rutile and its associations at Jolotca, Ditrau Alkaline Intrusive Massif, East Carpathians, Romania. *Proceedings of the Romanian Academy, Series B*, **17**, 39–55.

Kasama, T., Golla, U. and Putnis, A. (2003) High resolution and energy filtered TEM of the interface between hematite and ilmenite exsolution lamellae: relevance to the origin of lamellar magnetism. *American Mineralogist*, **88**, 1190–1196.

Kasama, T., McEnroe, S.A., Ozaki, N., Kogure, T. and Putnis, A. (2004) Effects of nanoscale exsolution in hematite–ilmenite on the acquisition of stable natural remanent magnetization. *Earth and Planetary Science Letters*, **224**, 461–475.

Mazzullo, L.J., Dixon, S.A. and Lindsley, D.H. (1975) T-fO_2 relationships in Mn-bearing Fe-Ti oxides. *Geological Society of America, Abstracts Program*, **7**, 1192.

McEnroe, S.A., Harrison, R.J., Robinson, P., Golla, U. and Jercinovic, M.J. (2001) Effect of fine-scale microstructures in titanohematite on the acquisition and stability of natural remanent magnetization in granulite facies metamorphic rocks, southwest Sweden: implications for crustal magnetism. *Journal of Geophysical Research*, **106**(B12), 30523–30546.

McEnroe, S.A., Harrison, R.J., Robinson, P. and Langenhorst, F. (2002) Nanoscale haematite–ilmenite lamellae in massive ilmenite rock: an example of lamellar magnetism with implications for planetary magnetic anomalies. *Geophysical Journal International*, **151**, 890–912.

McEnroe, S.A., Langenhorst, F., Robinson, P., Bromiley, G.D. and Shaw, C.S.J. (2004) What is magnetic in the lower crust? *Earth and Planetary Science Letters*, **226**, 175–192.

Mitchell, D.R.G. (2015) Development of an ellipse fitting method with which to analyse selected area electron diffraction patterns. *Ultramicroscopy*, **160**, 140–145.

Mitchell, R.H. and Liferovich, R.P. (2004) Ecandrewsite-zincian pyrophanite from lujavrite, Pilansberg alkaline complex, South Africa. *The Canadian Mineralogist*, **42**, 1169–1178.

Mitchell, R.H., Scott-Smith, B.H. and, Larsen, L.M. (1999) Mineralogy of ultramafic dikes from the Sarfartoq, Sisimiut and Maniitsoq areas, West Greenland. *Proceedings of the VII International Kimberlite Conference*, **2**, 574–583.

Mugnaioli, E., Capitani, G.C., Nieto, F. and Mellini, M. (2009) Accurate and precise lattice parameters by selected area electron diffraction in the transmission electron microscope. *American Mineralogist*, **94**, 793–800.

Robinson, P., Harrison, R.J., McEnroe, S.A. and Hargraves, R.B. (2002) Lamellar magnetism in the haematite–ilmenite series as an explanation for strong remanent magnetization. *Nature*, **418**, 517–520.

Robinson, P., Harrison, R.J., McEnroe, S.A. and Hargraves, R.B. (2004) Nature and origin of lamellar magnetism in the hematite–ilmenite series. *American Mineralogist*, **89**, 725–747.

Tarantino, S.C, Zema, M., Capitani, G.C., Scavini, M., Ghigna, P., Brunelli, M. and Carpenter, M.A. (2011) Rhombic-shaped nanodomains in columbite driven by contrasting cation order. *American Mineralogist*, **96**, 374–382.

Uher, P., Černý, P., Chapman, R., Határ, J. and Miko, O. (1998) Evolution of Nb,Ta-oxide minerals in the Prašivá granitic pegmatites, Slovakia. I. Primary Fe, Ti-rich assemblage. *The Canadian Mineralogist*, **36**, 525–534.

Wu, X., Qin, S. and Dubrovinsky, L. (2010) Structural characterization of the $FeTiO_3$–$MnTiO_3$ solid solution. *Journal of Solid State Chemistry*, **183**, 2483–2489.

Zaccarini, F., Garuti, G., Ortiz-Suarez, A. and Carugno-Duran, A. (2004) The paragenesis of pyrophanite from Sierra de Comechingones, Córdoba, Argentina. *The Canadian Mineralogist*, **42**, 155–168.

https://doi.org/10.1180/minmag.2016.080.154 Published online by Cambridge University Press